Numerical Investigation on the Comparability of Simulations and Experiments at the NACA 64418 Airfoil

Miguel Afonso Antunes

miguel.antunes@tecnico.ulisboa.pt

Instituto Superior Técnico, Universidade de Lisboa, Portugal

January 2021

Abstract

A measurement campaign was carried out at the Laminar Wind Tunnel of the IAG, regarding an extruded NACA64418 airfoil in low-speed stall conditions. Consequently, a numerical investigation on the influence of different turbulence models and boundary conditions for representing the tunnel walls is performed using the DLR TAU-Code as the flow solver. An initial RANS approach was undertaken and showed that the **symmetry plane** boundary condition, together with Menter's $k - \omega$ SST model, yielded the best agreement with the experiments. Particularly, concerning the separation pattern for $\alpha = 16°$, unlike the symmetry plane/SA and euler wall/SST combinations. Subsequently, a time resolved URANS approach with the symmetry plane/SST combination for 3 angles of attack ($\alpha = 8°, 12°, 16°$), showed an increased agreement with the experiments for the higher angles of attack. The spectral analysis and investigation of the wake's streamwise velocity and Reynolds stresses profiles revealed a periodic pumping motion of the stall, which could not be seen in the experiments, and the prediction of a more stable shear layer by part of the numerical approach. However, good qualitative agreement with the experiments was possible. Furthermore, the validity of the URANS approach was confirmed. Finally, investigations with the URANS approach for the **euler wall** condition revealed an inability to capture fluctuations that was solved with the use of hybrid RANS/LES methods. Adaptions of the grid for the **viscous wall** condition revealed a junction flow problem in the interaction between the wall's boundary layer and the wing, thus requiring further development.
Keywords: Computational Fluid Dynamics; Flow Separation; URANS; Turbulence.

1. Introduction

There is no doubt that accurate predictions of flow physics are essential in order to create efficient engineering solutions and for certain purposes, the prediction of flow separation, particularly, is a mandatory requirement to achieve this goal. The use of numerical methods to make these assessments is a key tool, however the flow in this regime is characterized by a complex, non-linear, transient behaviour and a compromise between available computational power and numerical methods is necessary. The use of experimental testing methods has always been the most direct path to make design decisions due to its ability of expanding the view over the phenomena that takes place for the given flow conditions. However, it also presents some limitations due to the role that wind tunnel walls play on the results, such as the effect of blockage. Besides these inherent limitations to wind tunnel testing, this approach is also an excellent way to make an assessment of the behaviour of different numerical methods. Through comparison between numerical results and experimental data, more knowledge can be gathered about the numerical models in question thus allowing to understand their strengths and limitations so that they can be applied in the right conditions and be further developed. An example of a complex flow behaviour can be found in the results from a measurement campaign on an extruded NACA 64418 airfoil in low-speed stall conditions, conducted in the Laminar Wind Tunnel (LWT) from the Institute of Aerodynamics and Gas Dynamics (IAG) of the University of Stuttgart. Representative and simplified flow cases such as the aforementioned are preferably used in numerical methods verification given that they significantly decrease the computational cost when compared with more complex geometries, such as full aircraft configurations, for example.

The need to pursue the improvement of numerical methods as a way to benefit sustainable development allied with the existence of a test case in the desirable regime, serves as the primary motivation for this work.

1.1. Objectives

The main objective of this work is to study the comparability between experimental wind tunnel results and numerical results regarding the complex, non-linear flow observed in low-speed stall conditions on an extruded NACA 64418 airfoil at a Reynolds number of 2.5×10^6. For the appropriate angles of attack, different models of the flow governing equations shall be used, namely the kω-SST and Spallart-Almaras, as well as different boundary conditions for representing the wind tunnel walls: **symmetry plane, euler wall and viscous wall**. As a starting point, a steady state RANS approach to the problem is used due to the fact that steady simulations are less time consuming, thus making it a fit approach for parametric studies. When unsteady nature phenomena is involved, it is not possible to capture it without time resolving methods, so the next step is taking a time resolving approach with URANS.

The statements regarding the comparability between results shall be made using the following quantitative and qualitative results available from the experimental test: force coefficients, pressure distributions, flow separation and stall cells, wake velocity and Reynolds stresses profiles, and spectral analysis on the streamwise velocity.

2. Literature Review and Fundamentals

2.1. Three Dimensional Flow Patterns in Stall Conditions

The post stall/on stall flow regime has been broadly investigated due to the sudden change of lift and drag as a consequence of flow separation. In an early study regarding such conditions, Winkelmand and Barlow [1] reported the existence of "owl shaped" structures on the suction side of their rectangular wing model through elementary flow visualization techniques and concluded that that the birth of such structures was not a tip effect but a consequence of a periodic breakdown of the separated region. Nowadays, according to the literature consensus, these structures are know as stall cells (SCs) and are described as a pair of symmetric counter-rotating swirling vortices, being the principal mean flow structures in this regime. Weihs and Katz [2] also laid down one of the first explanations for the appearance of this three dimensional structure attributing it to the result of a two dimensional separation line as a consequence of a Crow-type instability where a chain of vortex rings is formed through the interaction of two-counter rotating vortices that amplify small oscillations in their shape. The mechanism suggested by them is represented in Figure 1.

Among others, Zutskaya and Arieli [3] investigated stall cell behaviour using the RANS approach
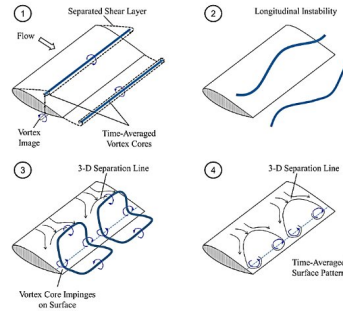

Figure 1: Stall cell formation mechanism as suggested by Weihs and Katz.

in parallel with experimental investigation. The numeric results showed a highly complex flowfield in the areas of reversed flow and it was found that the turbulence model had a quantitative influence without affecting the basic flow structure. Later, Manolesos et al. [4], also used the RANS approach to investigate on this matter in both two dimensional and three dimensional approaches. Their findings, at a $Re = 10^6$, showed a 3° delay in comparison with experimental data but, as in [3], qualitative analysis was also possible. In terms of force coefficients, due to delay in stall cell formation, an under prediction of the drag coefficient (C_D) was reported and the lift coefficient (C_L) was over predicted, although the trends in their evolution were similar to the experimental ones.

For this work, the available results from the experimental investigation also allowed to identify the presence of stall cells by means of flow visualization techniques. Given the low number of numerical research on the topic, this work aims to also provide some new information regarding the influence that different numerical approaches, namely time resolving ones, might have on the representation of such structures.

2.2. Fundamentals

2.2.1 Flow Solver

The DLR TAU-Code flow solver used for all the CFD analysis throughout this work is based on the compressible Navier-Stokes equations [5]. This set of equations is derived from the fundamental governing equations of fluid dynamics: the continuity, momentum and energy equations.

2.2.2 Governing Equations

When dealing with turbulent flows, the Reynolds decomposition technique is often used due to its decrease in both time and computational cost when compared with actually solving the Navier-Stokes equations.

The foundation for this method begins with the decomposition of the velocity in two components:

$$u = \bar{u} + u' \tag{1}$$

Where $\bar{u}$ denotes the mean value and u' the fluctuating component of velocity.

When dealing with a compressible medium, besides velocity and pressure fluctuations, density and temperature fluctuations must also to be taken into account [6]. The mechanism proposed by Reynolds, when applied to a compressible flow, introduces additional terms that significantly increase the complexity of the problem. To solve this, the density-weighted averaging procedure introduced by Favre ([7]) is applied. This method (denoted with the superscript ~) together with Reynold's, when applied to the continuity, momentum and energy equations results in the Favre-Reynolds Averaged Navier Stokes Equations:

$$\frac{\partial \bar{\rho}}{\partial t} + \frac{\partial}{\partial x_i}(\bar{\rho}\tilde{u}_i) = 0 \tag{2}$$

$$
\frac{\partial}{\partial t}(\bar{\rho}\tilde{u}_i) + \frac{\partial}{\partial x_j}(\bar{\rho}\tilde{u}_j\tilde{u}_i) \\
= -\frac{\partial p}{\partial x_i} + \frac{\partial}{\partial x_j}\left[\bar{\tau}_{ji} - \overline{\rho u_j'' u_i''}\right]
\tag{3}
$$

$$
\frac{\partial}{\partial t}\left[\bar{\rho}\left(\tilde{e} + \frac{\tilde{u}_i\tilde{u}_i}{2}\right) + \frac{\overline{\rho u_i'' u_i''}}{2}\right] + \\
\frac{\partial}{\partial x_j}\left[\bar{\rho}\tilde{u}_j\left(\tilde{h} + \frac{\tilde{u}_i\tilde{u}_i}{2}\right) + \tilde{u}_j\frac{\overline{\rho u_i'' u_i''}}{2}\right] = \\
\frac{\partial}{\partial x_j}\left[-\bar{q} - \overline{\rho u_j'' h''} + \overline{\tau_{ji}u_i''} - \overline{\rho u_j'' \tfrac{1}{2}u_i'' u_i''}\right] \\
\frac{\partial}{\partial x_j}\left[\tilde{u}_i\left(\bar{\tau}_{ij} - \overline{\rho u_i'' u_j''}\right)\right]
\tag{4}
$$

For this work, two eddy viscosity models were selected for the closure problem: the Spalart-Allmaras (SA), presented by Spalart and Allmaras [8] and the k-ω Shear Stress Transport (SST) developed by Menter [9] .

3. Experimental Measurements

The measurement campaign was conducted at the LWT from the Institute of Aerodynamics and Gasdynamics of the University of Stuttgart. The LWT, as described by [10], is an open return wind tunnel with a closed test section area of 0.73x2.73 m^2 and length of 3.15m.

For this campaign, several experiments were performed at two Reynolds numbers of $1.25{\times}10^6$ and $2.5{\times}10^6$ and at different angles of attack. In order to evaluate the flow's properties, the following techniques were used: Measurement of lift and drag polars, surface static pressure distributions, oil flow surface visualizations, hot-wire wake measurements and visualizations of the recirculation area by means of a high frequency camera and smoke injection. Further information regarding the particularities of each technique can be found in [10].

3.1. Mounting System

The model used in the experiments was obtained from the extrusion of a NACA 64418 airfoil. The chord length measures 0.6 meters and its span covers the full distance of 0.73 meters between the wind tunnel walls. The model was mounted vertically on the tunnel disc between the wind tunnel walls, as seen in Figure 2. The centre of the tunnel disc denotes the origin of the fixed tunnel coordinate system. The x-axis is in downstream direction, whereas the y-axis points to the suction side of the airfoil.

Figure 2: Wing Setup in the Laminar Wind Tunnel.

3.2. Wind Tunnel Corrections

Several effects related with the wind tunnel walls have an influence on the results. Thus, their contribution to the measured values has to be taken into account. D. Althaus, in his report [11], presents a description of the effects caused by solid blockage, streamline curvature, wake blockage as well as buoyancy, and how their are accounted for in the particular case of the LWT.

4. Numerical Setup

Prior to this work, a hybrid grid of the NACA 64418 testcase with the wingspan and chord length of the measurements in the LWT was created to meet the criteria for hybrid RANS/LES simulations by following guidelines as the ones presented in the report of Spalart [12]. The work developed using this grid was deemed satisfactory and therefore this hybrid grid was extended for the investigation of wall effects using steady and unsteady RANS calculations present in this work.

4.1. Grid Generation

The grid was generated by spanwise extrusion of a 2-D circular shaped grid centered at the airfoils's

leading edge and was composed by approximately 20 million cells. The circle has a radius of 50 times the chord length in order to guarantee that the inflow/outflow regions are sufficiently far away from the wing so that there is no influence from the wing at the boundaries. The width of the grid is equal to the wing's span $(0.73m)$ so that the wing extends from one boundary to the other as in the experimental test. The hybrid grid comprises a more refined, structured area covering the near wing and wake region and a coarser, prisms one, covering the remaining of the domain as shown in Figure 3. The structured block consists of approximately 14.7 million hexahedral elements with a characteristic cell size of $0.01m$ whereas the unstructured block is formed by approximately 5.3 million prism cells.
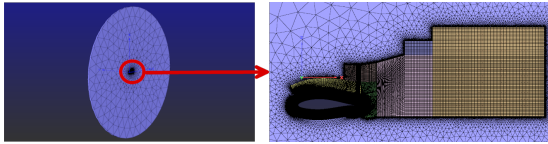

Figure 3: Grid.

The wing's surface is formed by approximatly 50000 cells equally spaced through 129 points in the spanwise direction and with a cell size of approximately $\Delta y/c = 0.0095$. The chordwise geometry was divided into 195 points. The leading edge and trailing edge areas, due to their geometric complexity, have a higher concentration of cells when compared with the remaining of the wing surface thus following the recommendations of the AIAA Drag Prediction Workshop [13] for chordwise spacing. It is worth noting that due to the increased computational cost associated with switching to three dimensional simulations, the chordwise and spanwise spacing is increased when compared with the two dimensional case.
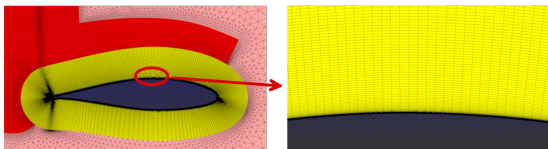

Figure 4: Hexahedron layers on wing surface.

When setting a no-slip condition on the airfoil surfaces, a higher resolution for the near wall cells is required in order to accurately capture the boundary layer physics and ensure a proper y^+ value on the viscous surfaces. For this purpose, a hexahedron layer consisting of 65 layers was extruded in the normal direction of the wing's surface (Figure 4).

4.2. Boundary Conditions

For this model, three regions need to be assigned a boundary condition type: the inflow/outflow region, the walls and the wing.

The inflow/outflow boundary was assigned the **farfield** option. This boundary condition defines an inflow/outflow boundary far away from the investigated configuration for external flow. With this boundary treatment, the presence of the configuration should hardly influence the state of the flow variables at the boundary as in an infinite domain (see [14]). For the inflow region, four variables have to be specified: the three velocity components and the temperature.

$$u = u_\infty, \quad T = T_\infty \quad (5)$$

The density, ρ, is extrapolated from the first inner grid point of the domain.

For the outflow region, the following condition is prescribed:

$$\rho = \rho_\infty \quad (6)$$

With the velocity and temperature values being extrapolated from the first inner grid point of the domain. Following this prescription of the flow conditions, the fluxes crossing the boundaries are computed by solving a Riemann problem [15].

The wing's surface was assigned the **viscous wall** boundary condition. This defines a solid wall that accounts for both viscid and inviscid effects. As noted in [16], the following overall constraints are defined at the wall when this boundary condition is set:

$$\vec{u} = 0, \quad (\vec{\nabla}T) \cdot \vec{n} = 0, \quad (\vec{\nabla}\rho) \cdot \vec{n} = 0 \quad (7)$$

For the modelling of the left and right wind tunnel walls, the **symmetry plane**, **euler wall** and **viscous wall** options were selected.

The **symmetry plane** boundary condition defines a plane respective to which the flow is symmetrical. This symmetry is handled by setting all fluxes in the wall-normal direction to zero. Notably, the following conditions are applied:

$$\vec{u} \cdot \vec{n} = 0, \quad (\vec{\nabla}T) \cdot \vec{n} = 0, \quad (\vec{\nabla}\rho) \cdot \vec{n} = 0 \quad (8)$$

When using the **euler wall** condition, a solid adiabatic wall is defined, identical to the viscous wall condition, however all viscous effects are neglected.

With the implementation of the **viscous wall** boundary condition to the tunnel walls a new problem arises. This boundary type implies the development of a boundary layer starting at the inlet of

4

our model therefore the distance between the flow-inlet boundary and the wing needs to be accounted for, as well as the cells resolution in the near-wall region. For this purpose, different grid adaptations of the one just presented were made, in order to fulfil the requirements for viscous walls.

4.3. Adjustments for Viscous Walls

In order to make the grid suitable for modelling the wind tunnel walls as viscous walls, increased resolution on the walls was necessary by means of a hexahedral layer extrusion. Several iterations of the grid were made, and the composition of the final one shall be described next.

The distance between the flow-inlet and the wing model was calculated based on the wall's boundary layer thickness, δ, when reaching the model. The value of δ, was not measured, but is estimated to be approximately 30 mm.For calculating the distance x from the wing to the flow-inlet, the Reynolds number for x (Re_x) was used together with the equation for the thickness of turbulent boundary layers along a flat plate. Substituting the known values into both equations yielded a value of $x = 1.975m$.

The calculation for the hexahedral layer's properties was performed with the aid of a python script for boundary layer mesh calculation and the inputs are listed in the table below.

Table 1: Inputs for prism and hexahedral layer calculation.

Desired y^+	1
Number of Prism Layers	45
Reynolds Number	2.5×10^6
Characteristic Length	$0.6m$

The structured region of the previous grid was kept and rotated accordingly to the desired angle of attack due to the new imposed boundary conditions that will be addressed. The circular domain was transformed into a rectangular one with a more uniform cell size, as shown in Figure 5, with a height of 40 times the chord lenght in both directions and and extension of 24 times the chord length downstream of the trailing edge. The final grid was composed by approximately 31 million cells.
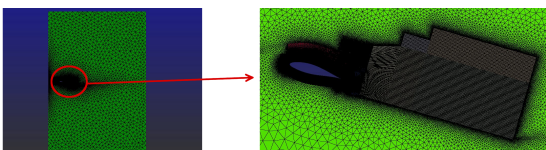

Figure 5: Grid for viscous walls condition.

The tunnel inlet wall was assigned the **engine exhaust** boundary condition which fixates the Mach number at the inlet whereas the outlet wall was assigned the **engine inflow** which is used to control the outlet's pressure in order to match the wind tunnel's reference pressure at the exit. The top and bottom walls were defined as non viscous walls (**euler wall** boundary condition).

4.4. Angle of Attack Selection

The angle of attack selection was based on the available data from the experiments, mainly the results provided by the polar measurements and the angles selected for the hot-wire runs (12° and 15°). For the steady RANS simulations, 9 different angles of attack were selected: 0°, 5°, 8°, 10°, 12°, 14°, 15°, 16° and 17°.

For the unsteady RANS simulations, one has to take into account the increased computational cost when compared with the steady version thus the angle of attack selection was narrowed to 3 angles (8°, 12° and 16°) in three different regimes of flow physics: onset of flow separation, initial stage of the separation and at a more advanced phase of flow separation.

4.5. Time Step Selection

The selection of the physical time step size for the unsteady calculations is based on the convective time scale of the flow. The reference length for the calculation of this scale is based on the chord length of the wing, $c = 0.6m$ and on the reference Mach number of $M_\infty = 0.185$. This results in a convective time scale of approximately $9.5 \times 10^{-3}s$. In combination with the spatial discretization, 100 time steps per convective time scale, resulted in a physical time step size of $9.5 \times 10^{-5}s$ which was used for all the URANS runs.

5. Results
5.1. RANS

Figure 6 shows the results obtained with the steady simulations for $\alpha = 16°$, together with the oil flow experiment.

The areas with a positive friction coefficient along the x axis ($Cf_x > 0$) are shown in red whereas the ones with $Cf_x < 0$ are represented in blue. The transition line between the red and blue area, depicts the separation front where $Cf_x = 0$ and the freestream flow is flowing along the x axis. The symmetry plane/SA and euler wall/SST combinations, showed in (b) and (c) respectively, although having the separation line maximum located just slightly above the experimental one, $x/c = 0.435$ for symmetry plane/SA and $x/c = 0.43$ for euler wall/SST, revealed to be inadequate in correctly predicting the separation
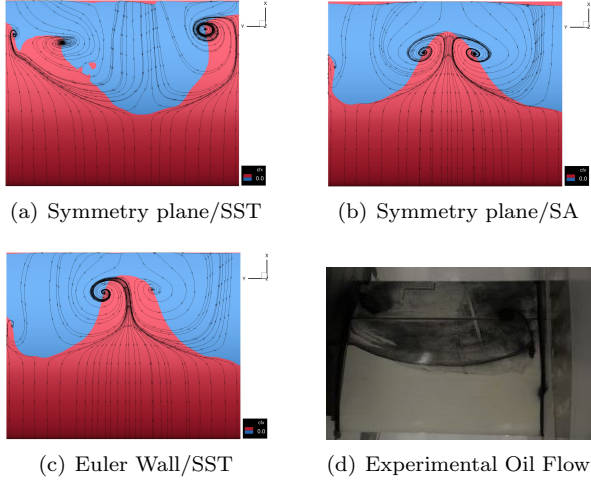
(a) Symmetry plane/SST

(b) Symmetry plane/SA

(c) Euler Wall/SST

(d) Experimental Oil Flow

Figure 6: Cf_x and streamlines on suction side for $\alpha = 16°$

pattern showed in (d), placing the pair of counter rotating vortices in the center of the wing and capturing a very different separation line shape. The symmetry plane/SST combination (figure 6 (a)), on the other hand, managed to more accurately reproduce the separation pattern. It showed a good agreement in the midspan region by placing the separation line maxima at approximately the $x/c = 0.42$ region with the deviations increasing as we move closer to the wall. However, three vortex structures can be identified on the surface whereas only two were reported from the experimental run. Given the better agreement when using the symmetry plane/SST combination, namely in terms o separation pattern, this setup was selected for the URANS simulations.

5.2. URANS

5.2.1 Separation Pattern

The unsteady run for the symmetry plane/SST combination at $\alpha = 16°$ revealed a strong periodic behaviour. The separation pattern for this case is shown in 7 for the local maxima and minima C_L values obtained in one cycle and for the mean streamwise friction coefficient, $\overline{Cf_x}$ in figure 8.
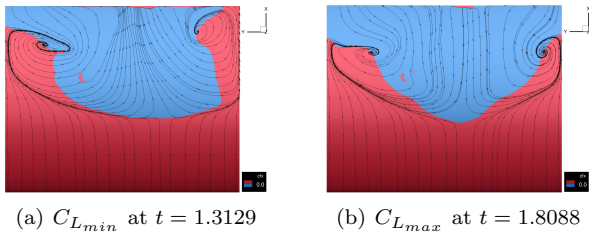

(a) $C_{L_{min}}$ at $t = 1.3129$

(b) $C_{L_{max}}$ at $t = 1.8088$

Figure 7: Cf_x and streamlines on suction side for $\alpha = 16°$
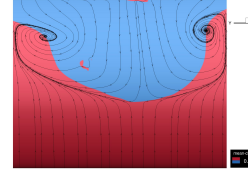

Figure 8: Mean Cf_x on suction side for $\alpha = 16°$.

Starting with an analysis of the mean values in 7 (c), the time resolving approach was able to "eliminate" the third vortex structure captured by the steady simulation and predict the formation of the counter rotating pair of vortices in the near wall region. The shape of the separation line remains similar to a one wave pattern, as in the experiments, however, it is pushed further downstream as we move closer to walls. The maximum of the separation line is located at $x/c = 0.42$ in the midspan region, as in its steady counterpart. An inspection of the Cf_x values for the local maximum and minimum C_L points within a cycle (in (a) and (b)) allows for a better understanding of the flow behaviour responsible for the pumping motion verified in the C_L value over time (figure 10). No distinctive differences were found in the position of the separation line maximum however, in the near wall region, the unsteady nature of the stall cell is quite visible when comparing the evolution of the vortex centres. Once the minimum value of C_L is attained, the stall cell progresses upstream while accompanying the curving of the separation line and increasing the C_L value until its maximum is reached, from where on, the inverse behaviour takes place. Although the predicted separation pattern is similar, the unsteadiness of the separation line diverges from the steady like behaviour found in the experiments, manifesting itself in a more intense manner on the right-hand side of the wing. Overall, the stall cell behaviour predicted on the wing, unlike in the experiments, pushes the separation line further downstream in the near wall region and is in part responsible for the high numerical C_L values verified in this regime.

5.2.2 Cp Distribution

For the $\alpha = 16°$ case, a better agreement was reached for the Cp distributions at the midspan position when using the time resolving approach. Figure 9 shows the results for the unsteady, steady and experimental runs. The Cp values plotted for the unsteady case are the mean values at the final time step of the run ($\overline{Cp}$). The mean suction peak value for the unsteady case ($\overline{Cp} = -6.7$), although still higher than the experimental one, improved when compared with the steady simulation.

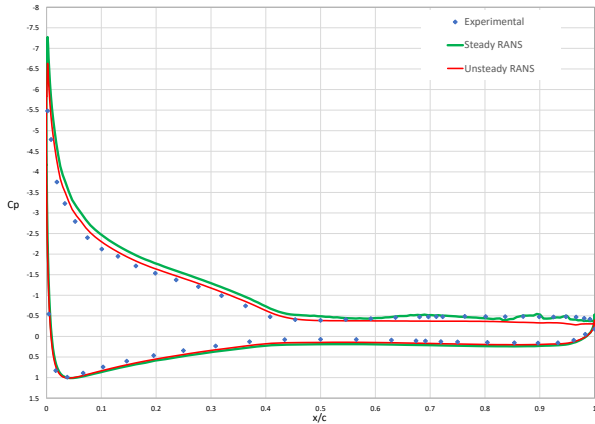In terms of the pressure side distribution, there

Figure 9: Mean Cf_x on suction side for $\alpha = 16°$.

Figure 10: Mean Cf_x on suction side for $\alpha = 16°$.

was a slight improvement as well but the more distinctive one took place on the suction side. The gap existent between $x/c = 0$ and $x/c = 0.6$ was shortened when switching to the time resolving method however, some accuracy was lost from $x/c = 0.6$ onwards. As is shown, the position associated with flow separation and at which the Cp values become constant, was predicted very closely to the experimental.

5.2.3 Force Monitors

For the $\alpha = 16°$ case, the flow conditions produced strong oscillations over time both in terms of C_L and C_D. However, this flow regime enabled the capture of a periodic behaviour, showing that URANS might be a good choice to simulate these flow conditions given that no medium scale fluctuations are present in the force coefficients. Starting from around $t = 1.4s$, the unsteady behaviour is almost fully established and behaving in cycles with an mean period of $\overline{\Gamma} = 0.092s$. The simulation can not be considered statistically converged as there are still oscillations in both the minimum and maximum values of C_L and C_D however, it can be deemed satisfying. This fact suggests that there might be a larger scale phenomena taking place that can not be captured by the current time step.

The mean C_L value for this case, taken from the point where the unsteadiness started to settle onwards is of $C_L = 1.385$ thus also decreasing in comparison with the steady calculations $C_{L_{steady}} = 1.54$ and moved closer to the experimental value $C_{L_{exp}} = 1.25$. Again, this mean C_L value is dependant on the time interval that one chooses to compute it but it is worth pointing out that even so, the mean C_L for this unsteady calculation will always be lower than the one from the steady calculations given the maximum value obtained ($C_L = 1.42$), therefore showing again the
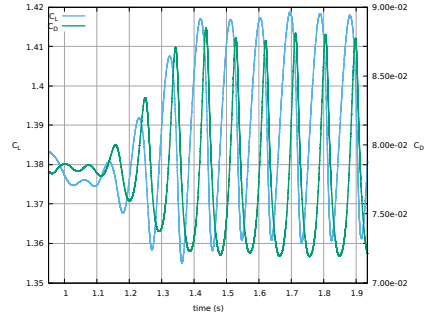
need of using time resolving methods for such flow conditions. When using the RANS approach, there is no guarantee that the turbulence model is able to filter every frequency, thus further investigation regarding the frequencies obtained is given later in section 5.2.5 by means of a spectral analysis.

5.2.4 Streamwise Velocity and Reynolds Stresses

The streamwise velocity and Reynolds stresses recorded during the wake hot-wire measurements were plotted, for each x position, together with the mean streamwise velocity ($\overline{u}$) profiles and Reynolds stresses from the unsteady symmetry plane/SST simulation at $\alpha = 16°$. For the 6 available x positions, two are located within the early separated shear layer, one near the trailing edge, two other in the middle part of the wake and the last one the furthest downstream. The results for the furthermost downstream position, at $x = 0.914m$ are shown in Figure 11

(a) $\overline{u}$

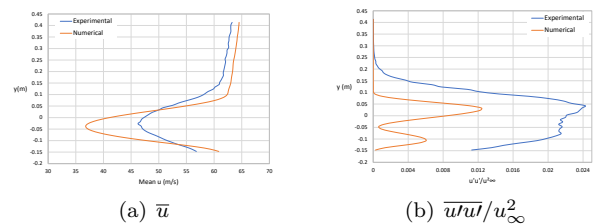(b) $\overline{u\prime u\prime}/u_\infty^2$

Figure 11: Wake Profiles at $x = 0.914m$

The experiments reported a velocity deficit with a magnitude and position that could be measured and two maxima present in the profile of Reynolds stresses that were likely associated with the upper and lower shear layers that delimit the extents of the recirculation region. The numerical results, were able to predict the wake streamwise velocity peak closely at the same position as the experiments, with $y = -26.8mm$ in the experiments versus $y = -37mm$ for the numerical however, the velocity deficit was over predicted with a thinner

7

velocity profile and stronger wake peak. In terms of Reynolds stresses, the numerical solution was able to predict the two peaks, with the stronger located closely at the same y position. The areas were the maxima of the Reynolds stresses are located, correspond to the higher velocity gradient, $\partial \overline{u}/\partial y$, in the velocity profiles, showing the outcome of a high turbulent shear. However, in quantative terms, the numerical results show a more stable shear layer, revealing a consequence of the URANS approach in not being able to predict the smaller scale eddies present in the flow.

For illustrative purposes, the position of the maximum velocity deficit in the wake was taken for each profile and plotted. As is shown in figure 12, the good agreement in the prediction of the velocity profile trends is well illustrated by the evolution of the wake's maximum velocity deficit point. It must be noted that the first two points depicted at $x = 0.211$ and $x = 0.311$ do not have the same meaning as the others since they are located within the separated shear layer and the hot wire probe is only able to measure the streamwise velocity magnitude.
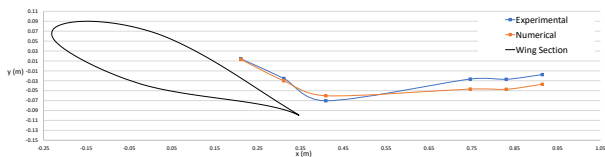

Figure 12: Mean Cf_x on suction side for $\alpha = 16°$.

5.2.5 Spectral Analysis on Streamwise Velocity

Welch's method, performed on the streamwise velocity, was used as a way to estimate the power spectral density (PSD). 3 points were selected to perform the analysis on the $\alpha = 16°$ numerical case, at the same location as in the experimental and the analysis for the point within the early separated shear leayer is shown in figure 13. For the numerical case, 8800 time samples were used (from $t = 1.1001s$ to $t = 1.9361s$) and the results were plotted in terms of power spectral density (PSD) over the Strouhal number (Sr)

The spectral analysis for the experimental data reveals in all cases a PSD plateau located in the low Sr range. In the early separated region at $x = 0.211m$ shown in figure 13 (b), the experimental spectrum shows low frequency peaks, that were linked with the hot wire mount oscillations verified in the experiments. The -5/3 slope of the inertial subrange of the turbulent cascade was well captured for all the experimental runs.

In terms of numerical results, for all positions such as the one depicted in figue 13 (a), the PSD values take lower order magnitudes than the experimental ones, this can correlate with the higher Reynolds stresses values captured in the experiments reflecting stronger fluctuations thus a higher PSD value. A strong amplification was verified at $Sr = 0.10258$. This peak translates into a period of approximately $\Gamma = 0.0929s$, matching the average period $\overline{\Gamma}$ verified for the cycles in the time series (figure 10) which is associated with the movement of the stall cells thus reflecting the dominance of this stall cell pumping motion in the flow field. The following peaks represent the 2nd, 3rd and 4th harmonics of this amplification. The captured peak at $Sr = 0.10258$ in the numerical simulations as a result of the SC induced pumping motion, differs from the plateau found in the experiments that, albeit revealing an elevation of the PSD in the same region, did not show any dominant frequency. This, together with the fact that an essentially stationary separation line was verified during the experiments, raises the question if weather the predicted periodic motion is realistic or not. It is also possible that, in the experiments, different low frequency phenomena that was not predicted by the numerical approach overlapped, with its superimposition resulting in the reported PSD plateau.

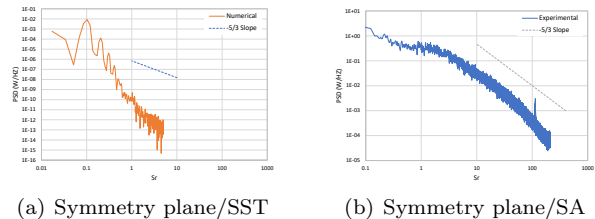(a) Symmetry plane/SST

(b) Symmetry plane/SA

Figure 13: PSD of the streamwise velocity at $x = 0.211$

The difference in the scale of frequencies between numerical and experimental might be associated not only with the inability of URANS to capture higher frequencies but also with the PSD method and time sampling. The larger differences in the experimental results were obtained at lower Sr values and are therefore associated with lower frequency phenomena. The time samples were collected for approximately 10 seconds while the simulation time for this case was of approximately 1.94 seconds. Thus, the experimental time series will be able to capture larger scale events than the numerical one. Further, for the numerical results, as expected, the -5/3 slope of the inertial subrange of the turbulent cascaded was not captured given also that some of the frequencies are filtered by URANS.

5.2.6 Remarks on Euler Walls and Viscous Walls

An attempt to implement the combination of Euler Walls with the URANS approach using both the SST and SA model was made for the cases of $\alpha = 12°$ and $\alpha = 16°$. When using this setup, the solution, over time, reflected the absence of barely any fluctuations. When strong unsteady behaviour was expected at the highest angles of attack, this combination was unable to capture them even with a considerable simulation time.
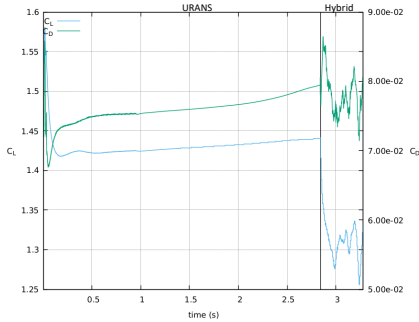

Figure 14: Mean Cf_x on suction side for $\alpha = 16°$.

The reason for this behaviour remains unkonw, but an attempt to tackle this problem and verify the setup conditions was made by switching to a higher resolution method: hybrid RANS/LES. Applying this mode to the same conditions allowed to capture fluctuations within the flow field as depicted in figure 14 hinting that the damping of the solution was not a setup problem but it instead originated in the combination of the boundary condition with the turbulence model. From the beginning the model used was URANS SST, and from around $t = 2.8s$ onwards, the flow field was solved using the hybrid method and fluctuations were captured as expected in these conditions. Although not many conclusions can be drawn from the small time series captured with the hybrid mode, it does indicate an initial better suitability of this higher resolution method when compared with URANS, in terms of capturing time dependant phenomena for this particular combination.

Different approaches were also taken regarding the grid to enable the modelling of the wind tunnel walls as viscous walls. The results from the final approach, as described in section 4 is shown.

The junction flow problem consequences between the wing and the walls, as in the previous approaches, are very present by revealing a large separated flow region in this area as depicted by the streamwise friction coefficient plotted in figure 15. In (a) the suction side perspective is shown and in (b) the wall's perspective at $y/b = 1$. Unlike in the experiments, the separation is still strongly influ-
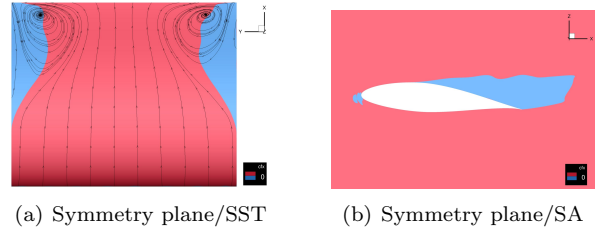

(a) Symmetry plane/SST   (b) Symmetry plane/SA

Figure 15: Cf_x and streamlines for $\alpha = 5°$

enced by the walls and an evaluation of the boundary thickness size revealed a value of approximately $80mm$, which is quite large when compared with the estimated experimental value of $30mm$. The large separated region verified in these conditions, reflected itself on the low lift coefficient obtained of $C_L = 0.51$ when compared with the experimental of $C_L = 0.91$. However, in percentual terms, we see an improve from the original grid were the deviation to the experimental lift was approximately 47% whereas in this case it is of 43%. The assumption of fully turbulent conditions made by the model, raises the question of their suitability when dealing with this type of conditions as well as the assumption of isotropic turbulence and modelling of the Reynolds stresses also has a strong influence in the outcome of the simulations.

6. Conclusions and Recomendations for Future Work

The results obtained are of interest to evaluate the performance of different boundary conditions and turbulence models implemented in the DLR TAU Code. It was observed that RANS yields very satisfying predictions for low angles of attack, but once the angle of attack increased to values where flow separation occurs, the discrepancy to the experimental results begins due to the assumption of fully turbulent conditions. However, the use of steady RANS, given its faster computation time, revealed to be a good approach in terms of parametric studies with the symmetry plane/SST combination yielding the most satisfying results, mainly in terms of separation pattern, as a reference for the subsequent time resolving approach.

The need of using time resolving methods when dealing with flow conditions involving large separation regions was shown by means of the increasing agreement with the experiments when switching to URANS. Both the C_L values and the mean Cp distributions became closer to the experimental ones, as well as the separation pattern. The unsteady nature of stall cells was captured, and at $\alpha = 16°$ it was possible to identify it as the reason for the pumping motion verified in the time series. The wake analysis of the flow managed to predict some of the trends in the wake streamwise

velocity and Reynolds stresses profiles but revealed a strong discrepancy in quantitative terms. The spectral analysis showed the validity of the URANS approach by revealing the captured fluctuations as a low frequency behaviour and predicting a fast decay towards the higher frequencies which hints at a spectral gap between resolved and modelled turbulence. Overall, URANS combined with the symmetry plane/SST case, revealed itself to be useful in predicting qualitative aspects of the flows physics but higher resolution methods are necessary. It was found that URANS was unable to capture a suitable range of the flow's unsteadiness when using the euler wall boundary condition either with the SST or SA models. This problem was solved by switching to the higher resolution method hybrid RANS/LES with which fluctuations began being captured. The viscous wall case posed the particularity of having to account for the boundary layer that is formed on the walls and its interaction with the wing. Several iterations of the numerical setup were made however, the junction flow condition between the walls and the wing still shows poor resolution.

6.1. Future Work

Future work on this case should focus on higher resolution methods, i.e. hybrid RANS/LES as a way to deal with the frequencies that URANS cannot capture. A starting point to consider could be using the symmetry plane condition and afterwards progress to the euler wall boundary condition. Investigating the time step size by decreasing it to half of the value used for this work should also be considered. Further more, additional effort should be made in the numerical setup for the viscous walls and the possibility of using a Reynolds Stress Transport model should be contemplated given that it directly resolves the Reynolds stresses instead of modelling them.

References

[1] Allen E. Winkelman and Jewell B.Barlow. Flowfield Model for a Rectangular Planform Wing beyond Stall. *AIAA Journal*, 18(8):1006–1008, August 1980.

[2] Daniel Weihs and Joseph Katz. Cellular patterns in poststall flow over unswept wings. *AIAA Journal*, 21(12):1757–1759, December 1983.

[3] T. Zarutskaya and R. Arieli. On Vortical Flows Structures at Wing Stall and Beyond. In *AIAA 35th Fluid Dynamics Conference and Exhibit*, Toronto, Ontario, Canada, June 2005.

[4] Marinos Manolesos, Georgios Papadakis, and Spyros G. Voutsinas. Experimental and computational analysis of stall cells on rectangular wings. *Wind Energy*, 17(6):939–955, June 2014.

[5] Jr John D. Anderson. *Computational Fluid Dynamics: The Basics With Applications.* McGraw-Hill Series in Mechanical Engineering, 1995.

[6] David C. Wilcox. *Turbulence Modeling for CFD.* DCW Industries, Inc., 1993.

[7] A. Favre. Equations de Gaz Turbulents Compressibles. *Journal de Mecanique*, 4(3):361–390, 1965.

[8] P. R. Spalart and S. R. Allmaras. A one-equation turbulence model for aerodynamic flows. In *AIAA 30th Aerospace Sciences Meeting and Exhibit*, Reno, NV, USA, January 1992.

[9] F. R. Menter. Zonal two equation k-ω turbulence models for aerodynamic flows. In *AIAA 24th Fluid Dynamics Conference*, Orlando, FL, USA, July 1993.

[10] W. Würz, A. Herrig, M. Kamruzzamann, and A. Ivanov. *Measurements of normal-to-wall and spanwise integral correlation lengths at the trailing edge of the NACA 643-418.* IAG - University of Stuttgart, 2008.

[11] D.Althaus. Tunnel-wall corrections at the laminar wind tunnel. Technical report, IAG - University of Stuttgart, 2003.

[12] Philippe R. Spalart. Young-person's guide to detached-eddy simulation grids. Contractor Report NASA/CR-2001-211032, Boeing Commercial Airplanes, Seattle, WA, USA, July 2001.

[13] 6th AIAA Cfd Drag Prediction Workshop. https://aiaa-dpw.larc.nasa.gov/.

[14] Deutsches Zentrum fur Luft- und Raumfahrt e.V - Institute of Aerodynamics and Flow Technology. *TAU-Code User Guide*, release 2018.1.0 edition, July 2018.

[15] Laia Alcaraz Capsada. Simulation of atmospheric eeffects with the dlr code tau. Master's thesis, Universitat Politecnica de Catalunya, 2015.

[16] Christoph Wolf. *A Chimera Simulation Method and Detached Eddy Simulation for Vortex-Airfoil Interactions.* PhD thesis, Georg-August-Universität Göttingen, 2010.